

Central-Upwind Scheme for the Phase-Transition Traffic Flow Model

Shaoshuai Chu*, Alexander Kurganov†, Saeed Mohammadian‡ and Zuduo Zheng§

Abstract

Phase-transition models are an important family of non-equilibrium continuum traffic flow models, offering properties like replicating complex traffic phenomena, maintaining anisotropy, and promising potentials for accommodating automated vehicles. However, their complex mathematical characteristics such as discontinuous solution domains, pose numerical challenges and limit their exploration in traffic flow theory. This paper focuses on developing robust and accurate numerical methods for phase-transition traffic flow models. The paper proposes a second-order semi-discrete central-upwind scheme, specifically designed for discontinuous phase-transition models. This novel scheme incorporates the projection onto appropriate flow domains, ensuring enhanced handling of discontinuities and maintaining physical consistency and accuracy. The paper demonstrates the efficacy of these schemes through extensive and challenging numerical tests, showcasing their potential to facilitate further research and application in phase-transition traffic flow modeling. The ability of phase-transition models to embed the “time-gap”—a crucial element in automated traffic control—as a conserved variable, aligns seamlessly with the control logic of automated vehicles, presenting significant potential for future applications, and the proposed numerical scheme now substantially facilitates exploring such potentials.

Key words: Finite-volume central-upwind schemes, phase-transition traffic flow model, free traffic flow, congested traffic flow

AMS subject classification: 76M12, 65M08, 76A30, 76T99, 35L65.

1 Introduction

Continuum models treat traffic flow as a compressible fluid and analyze its dynamics using aggregated state variables like flow and density, proving beneficial in real-world traffic management and

*Department of Mathematics and Shenzhen International Center for Mathematics, Southern University of Science and Technology, Shenzhen, 518055, China; chuss@mail.sustech.edu.cn

†Department of Mathematics, Shenzhen International Center for Mathematics and Guangdong Provincial Key Laboratory of Computational Science and Material Design, Southern University of Science and Technology, Shenzhen, 518055, China; alexander@sustech.edu.cn

‡School of Civil Engineering, the University of Queensland, Brisbane Qld, 4072, Australia; s.mohammadian@uq.edu.au

§School of Civil Engineering, the University of Queensland, Brisbane Qld, 4072, Australia; zuduo.zheng@uq.edu.au

control [20]. Over time, a variety of continuum models have been developed, each incorporating different empirical and behavioral characteristics of traffic flow [21]. These models are generally classified into two main categories: equilibrium and non-equilibrium models. Equilibrium models are based on flow conservation principles, consistently linking speed and density without time or space differentiation. In contrast, non-equilibrium models use separate dynamic partial differential equations (PDEs) for speed and density, with their universal relationship only applicable in steady-state equilibrium, irrespective of time and space.

Non-equilibrium continuum traffic flow models are crucial for analyzing traffic dynamics, including the development and spread of persistent waves from initial disturbances to near-equilibrium conditions. To be well-defined, these models must meet the following three criteria:

- Adherence to causality laws, implying that drivers respond to stimuli ahead of them, and thus, characteristic traffic waves, generated by the model, must not exceed average traffic speeds due to this directional response [8];
- Considering the fact that the negative correlation between driver speed and intervehicular spacing restricts macroscopic traffic conditions between specific paths on the flow-density diagram, the model must ensure that traffic states stay within these viable trajectories and automatically satisfy the consistency conditions such as zero speed at maximum density [27];
- Distinct representation of the dynamics in free-flow and congested phases, ensuring that phenomena unique to each phase are accurately simulated and exclusive to that phase [14].

To the best of our knowledge, phase-transition models of traffic flow, initially proposed in [5] and further developed in [2, 7], represent the only class of non-equilibrium models that endogenously meet all of the aforementioned three criteria. The models in this family consider distinct hyperbolic equations for the free-flow and congestion phases, respectively. In the free-flow phase, a simplified equilibrium model with traffic speed being a direct function of density is used, while for the congestion phase, a 2×2 hyperbolic system is employed, linking density and speed through a conserved variable, which is equivalent to the inverse of the average time gap.

The family of phase-transition are promising from a physical perspective in several regards. An empirical study comparing empirical vehicle trajectories has demonstrated the efficacy of phase-transition models in replicating various complex traffic phenomena, including traffic hysteresis and the convective propagation of congested states [1]. Furthermore, phase-transition traffic flow models introduced in [6] and [2] are excellent foundational models for extension to accommodate the governing principles of Connected and Automated Vehicles (CAVs). This suitability stems from the fact that the time-gap, an essential decision variable used in the control laws of CAVs, is already directly incorporated as a conserved variable in these models.

Nevertheless, the significant potential of phase transition models has been overlooked in the traffic flow theory literature, especially concerning numerical simulations and analysis. This research gap can be attributed to the inherent mathematical complexity of these models, which makes them very challenging to simulate numerically using the existing numerical schemes. We can only refer the reader to [3], where a Godunov-type method for a phase-transition model was proposed. In this method, mesh cells along phase boundaries are adjusted for accurate projections and a Glimm-type sampling technique post-projection is employed to preserve the numerical solution's integrity. We stress that the Godunov scheme and other Godunov-type upwind schemes rely on (approximately) solving the (generalized) Riemann problems arising at each cell interface. This

introduces significant complexity, primarily due to extensive conditional logic for determining the nature of the solution—shock waves, rarefaction waves, or contact discontinuities—based on local conditions. This detailed, case-by-case approach significantly increases computational complexity and overhead, rendering Godunov-type upwind schemes less practical for large-scale applications.

This paper aims to bridge the aforementioned research gap by developing a numerical scheme that overcomes the aforementioned difficulties. The contributions of this study are two-fold. First, we aim to develop a novel, accurate, and robust numerical scheme and demonstrate its performance in solving the Riemann problems across a comprehensive range of challenging scenarios. Second, we utilize the proposed scheme to shed light on the phase-transition model's behavior in a wide range of physically tangible real-world traffic scenarios.

The proposed numerical scheme is based on further development of the second-order semi-discrete central-upwind (CU), which were introduced in [15–17] as a "black-box" solver for general hyperbolic systems of conservation laws. In this paper, we incorporate novel mechanisms to tailor the CU scheme for discontinuous phase-transition models, ensuring physical consistency and accuracy by projecting computed results onto the correct flow domains. To demonstrate the performance of the proposed scheme, extensive and challenging numerical tests are conducted. Furthermore, after sufficiently demonstrating the scheme's performance for Riemann problems, we implement the phase-transition traffic flow model in several complex scenarios, aiming to elaborate on the physical interpretation of the proposed model.

The rest of the paper is organized as follows. In §2, we describe the phase-transition traffic flow model. In §3, we introduce the designed numerical method for the studied model. Finally, in §4, we apply the developed scheme to a number of numerical examples. We demonstrate that the proposed scheme can capture the solution sharply and in a non-oscillatory manner.

2 Phase-Transition Traffic Flow Model

^(sec2) The phase-transition model, which was initially proposed in [5] (see also [6,7]), couples two different traffic flow models. In the free-flow domain, where the traffic density ρ is smaller than a given threshold ρ_{cr}^f , the following scalar equation for ρ is used:

$$\rho_t + (\rho V_f(\rho))_x = 0, \quad (2.1) \quad \boxed{2.1}$$

where V_f is the traffic speed in free flow. In the congested-flow domain, where $\rho > \rho_{cr}^f$, the following second-order traffic flow model is utilized:

$$\begin{cases} \rho_t + (\rho V_c(\rho, q))_x = 0, \\ q_t + ((q - q^*) V_c(\rho, q))_x = 0, \end{cases} \quad (2.2) \quad \boxed{2.2}$$

where V_c is the traffic speed in congested regions. In (2.1) and (2.2), x is the spatial variable, t is time, q is a flow-type variable, q^* is a constant flow-type characteristic parameter, and the functions V_f and V_c are given by

$$V_f(\rho) = V_{max}, \quad V_c(\rho, q) = \left(1 - \frac{\rho}{\rho_{max}}\right) \frac{q}{\rho} \quad (2.3) \quad \boxed{2.3}$$

with V_{max} and ρ_{max} being the maximum speed and density.

We notice that q is neither defined nor used in (2.1), but in order to treat the model transition regions, we need to introduce q in the free-flow domain. This is done by substituting $V_c(\rho, q) = V_{max}$ into (2.3), which results in

$$q(\rho) = \frac{V_{max}}{\frac{1}{\rho} - \frac{1}{\rho_{max}}}. \quad (2.4) \quad \boxed{2.4}$$

Both the free and congested domains can be schematically presented in the (ρ, q) -plane; see Figure 2. In this figure:

- The curve L_f satisfying (2.4) for $\rho \in [0, \rho_{cr}^f]$ represents the free domain.
- The domain Ω_c , which is bounded by the curves L_1 , L_2 , L_3 , and the line $\rho = \rho_{max}$ represents the congested-flow domain.

One can show that if the solution is inside either free or congested domain, it will stay there and phase transition is possible only at the boundaries between the free and congested domains [6].

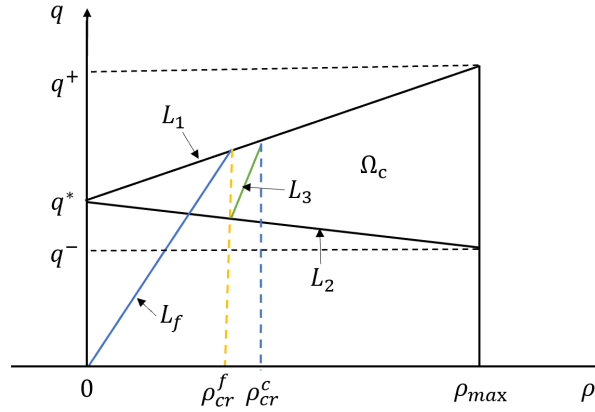


Figure 2.1: (ρ, q) -diagram of the phase-transition traffic flow model.

⟨fig1⟩ The three curves used in the definition of Ω_c are

$$L_1 : q = q^* + \frac{q^+ - q^*}{\rho_{max}} \rho, \quad L_2 : q = q^* + \frac{q^- - q^*}{\rho_{max}} \rho, \quad L_3 : q = \frac{\rho \rho_{max}}{\rho_{max} - \rho} V_{c+},$$

where q^\pm are the maximum/minimum admissible values for q and V_{c+} is the maximum speed in congested domain. The curves L_1 and L_3 intersect at the point with

$$\rho = \rho_{cr}^c := \frac{2\rho_{max}q^*}{\rho_{max}V_{c+} + 2q^* - q^+ + \sqrt{(\rho_{max}V_{c+} + 2q^* - q^+)^2 + 4(q^+ - q^*)q^*}}.$$

Finally, we note that one can put the system (2.1)–(2.3) to the following vector form:

$$\mathbf{U}_t + \mathbf{F}(\mathbf{U})_x = \mathbf{0}, \quad (2.5) \quad \boxed{2.5}$$

where

$$\mathbf{U} = \begin{pmatrix} \rho \\ q \end{pmatrix} \quad \text{and} \quad \mathbf{F}(\mathbf{U}) = \begin{cases} (\rho V_{max}, q V_{max})^\top & \text{if } (\rho, q) \in L_f, \\ (\rho V_c, (q - q^*) V_c)^\top & \text{if } (\rho, q) \in \Omega_c. \end{cases} \quad (2.6) \quad \boxed{2.6}$$

We stress that for the free-flow domain, the equation for q will not be numerically solved, but the vector form (2.5)–(2.6) will be convenient for the presentation of the numerical method in the next section.

3 Numerical Method

^(sec3) In this section, we develop the second-order semi-discrete CU scheme for the studied phase-transition traffic flow model.

We cover the computational domain with the uniform cells $C_j := [x_{j-\frac{1}{2}}, x_{j+\frac{1}{2}}]$ of size Δx centered at $x_j = (x_{j-\frac{1}{2}} + x_{j+\frac{1}{2}})/2$ and denote by $\bar{\mathbf{U}}_j(t)$ the computed cell averages of $\mathbf{U}(\cdot, t)$ over the corresponding intervals C_j , namely,

$$\bar{\mathbf{U}}_j(t) := \frac{1}{\Delta x} \int_{C_j} \mathbf{U}(x, t) dx.$$

We suppose that at a certain time $t \geq 0$, the cell averages $\bar{\mathbf{U}}_j(t)$ are available and they all belong to either L_f and Ω_c (see Figure 2). Note that $\bar{\mathbf{U}}_j$ and many other indexed quantities, which will be introduced below, are dependent and from here on we will suppress this time-dependence for the sake of brevity.

In the semi-discrete framework, the numerical solution of (2.5)–(2.6) is evolved in time by solving the following system of ODEs:

$$\frac{d\bar{\mathbf{U}}_j}{dt} = -\frac{\mathcal{F}_{j+\frac{1}{2}} - \mathcal{F}_{j-\frac{1}{2}}}{\Delta x}, \quad (3.1) \quad \boxed{3.2}$$

where the CU numerical flux $\mathcal{F}_{j+\frac{1}{2}}$ is given by [16]

$$\mathcal{F}_{j+\frac{1}{2}} = \frac{a_{j+\frac{1}{2}}^+ \mathbf{F}(\mathbf{U}_{j+\frac{1}{2}}^-) - a_{j+\frac{1}{2}}^- \mathbf{F}(\mathbf{U}_{j+\frac{1}{2}}^+)}{a_{j+\frac{1}{2}}^+ - a_{j+\frac{1}{2}}^-} + \frac{a_{j+\frac{1}{2}}^+ a_{j+\frac{1}{2}}^-}{a_{j+\frac{1}{2}}^+ - a_{j+\frac{1}{2}}^-} \left(\mathbf{U}_{j+\frac{1}{2}}^+ - \mathbf{U}_{j+\frac{1}{2}}^- - \mathbf{Q}_{j+\frac{1}{2}} \right). \quad (3.2) \quad \boxed{3.3}$$

Here, $\mathbf{U}_{j+\frac{1}{2}}^\pm$ are the right- and left-sided point values of \mathbf{U} at the cell interface $x = x_{j+\frac{1}{2}}$ obtained with the help of a conservative, second-order accurate, and non-oscillatory piecewise linear reconstruction.

We use different reconstructions in the free domain away from the phase-transition areas (Domain I), in the congested domain away from the phase-transition areas (Domain II), and in the phase-transition areas consisting of the six cells (three on the left and three on the right) around each interface between the free- and congested-flow domains (Domain III).

In Domain I, we only need to compute the one-sided point values $\rho_{j+\frac{1}{2}}^\pm$. To this end, we apply the generalized minmod reconstruction (see Appendix A) to the density ρ with $\theta = 1.5$ in (A.2). In Domain III, we reconstruct both $\rho_{j+\frac{1}{2}}^\pm$ and $q_{j+\frac{1}{2}}^\pm$ using the same minmod limiter from Appendix A but with $\theta = 1$ in (A.2) now applied to both ρ and q . Note that here we use a smaller value of θ to minimize possible oscillations in the interface areas. In Domain II, applying the minmod limiter to the ρ - and q -component of the computed solution may lead to relatively large oscillations. In order to suppress them, we apply the minmod limiter with $\theta = 1.5$ in (A.2) to the local characteristic variables, which are obtained using the local characteristic decomposition (see, e.g., [9, 12, 13, 19, 23–25, 28] and references therein); see Appendix B for details.

Remark 3.1 We detect the interface using the following simple approach: if $(\bar{\rho}_J - \rho_{cr}^f)(\bar{\rho}_{J+1} - \rho_{cr}^f) \leq 0$, then $x = x_{J+\frac{1}{2}}$ is the interface, and cells C_{J-2}, \dots, C_{J+3} belong to Domain III.

After reconstructing the point values $(\rho_{j+\frac{1}{2}}^\pm, q_{j+\frac{1}{2}}^\pm)$, we modify them unless $(\rho_{j+\frac{1}{2}}^\pm, q_{j+\frac{1}{2}}^\pm) \in L_f$ or $(\rho_{j+\frac{1}{2}}^\pm, q_{j+\frac{1}{2}}^\pm) \in \Omega_c$. The details on the proposed modification (projection) onto L_f/Ω_c can be founded in §3.1.

In (3.2), $a_{j+\frac{1}{2}}^\pm$ are the one-sided local speeds of propagation, which can be estimated using the largest (λ_2) and the smallest (λ_1) eigenvalues of the Jacobian $A = \frac{\partial \mathbf{F}}{\partial \mathbf{U}}$. This can be done as follows (see, e.g., [15, 16]):

$$a_{j+\frac{1}{2}}^+ = \max \left\{ \lambda_2(\mathbf{U}_{j+\frac{1}{2}}^-), \lambda_2(\mathbf{U}_{j+\frac{1}{2}}^+), 0 \right\}, \quad a_{j+\frac{1}{2}}^- = \min \left\{ \lambda_1(\mathbf{U}_{j+\frac{1}{2}}^-), \lambda_1(\mathbf{U}_{j+\frac{1}{2}}^+), 0 \right\}. \quad (3.3) \quad \boxed{3.3a}$$

Computing $a_{j+\frac{1}{2}}^\pm$ according to (3.3) requires, however, considering four possible cases depending on whether the left and right reconstructed states $\mathbf{U}_{j+\frac{1}{2}}^\pm$ are in free or congested domain as in the free-flow domain the eigenvalues of A are $\lambda_1^f = \lambda_2^f = V_{max}$ and in the congested-flow domain

$$\lambda_1^c = (q - q^*) \left(\frac{1}{\rho} - \frac{2}{\rho_{max}} \right) - \frac{q^*}{\rho_{max}}, \quad \lambda_2^c = V_c(\rho, q).$$

We then obtain:

- If both $(\rho_{j+\frac{1}{2}}^\pm, q_{j+\frac{1}{2}}^\pm) \in \Omega_c$, we take

$$a_{j+\frac{1}{2}}^+ = \max \left\{ \lambda_2^c(\mathbf{U}_{j+\frac{1}{2}}^-), \lambda_2^c(\mathbf{U}_{j+\frac{1}{2}}^+), 0 \right\}, \quad a_{j+\frac{1}{2}}^- = \min \left\{ \lambda_1^c(\mathbf{U}_{j+\frac{1}{2}}^-), \lambda_1^c(\mathbf{U}_{j+\frac{1}{2}}^+), 0 \right\};$$

- If both $(\rho_{j+\frac{1}{2}}^\pm, q_{j+\frac{1}{2}}^\pm) \in L_f$, we take

$$a_{j+\frac{1}{2}}^+ = V_{max}, \quad a_{j+\frac{1}{2}}^- = 0;$$

- If $(\rho_{j+\frac{1}{2}}^-, q_{j+\frac{1}{2}}^-) \in \Omega_c$ and $(\rho_{j+\frac{1}{2}}^+, q_{j+\frac{1}{2}}^+) \in L_f$, we take

$$\begin{aligned} a_{j+\frac{1}{2}}^+ &= \max \left\{ \lambda_2^c(\mathbf{U}_{j+\frac{1}{2}}^-), \lambda_2^f(\mathbf{U}_{j+\frac{1}{2}}^+), 0 \right\} = \max \left\{ \lambda_2^c(\mathbf{U}_{j+\frac{1}{2}}^-), V_{max}, 0 \right\} = V_{max}, \\ a_{j+\frac{1}{2}}^- &= \min \left\{ \lambda_1^c(\mathbf{U}_{j+\frac{1}{2}}^-), \lambda_1^f(\mathbf{U}_{j+\frac{1}{2}}^+), 0 \right\} = \min \left\{ \lambda_1^c(\mathbf{U}_{j+\frac{1}{2}}^-), V_{max}, 0 \right\} = \min \left\{ \lambda_1^c(\mathbf{U}_{j+\frac{1}{2}}^-), 0 \right\}; \end{aligned} \quad (3.4) \quad \boxed{3.4a}$$

- If $(\rho_{j+\frac{1}{2}}^-, q_{j+\frac{1}{2}}^-) \in L_f$ and $(\rho_{j+\frac{1}{2}}^+, q_{j+\frac{1}{2}}^+) \in \Omega_c$, we take

$$\begin{aligned} a_{j+\frac{1}{2}}^+ &= \max \left\{ \lambda_2^f(\mathbf{U}_{j+\frac{1}{2}}^-), \lambda_2^c(\mathbf{U}_{j+\frac{1}{2}}^+), 0 \right\} = \max \left\{ V_{max}, \lambda_2^c(\mathbf{U}_{j+\frac{1}{2}}^+), 0 \right\} = V_{max}, \\ a_{j+\frac{1}{2}}^- &= \min \left\{ \lambda_1^f(\mathbf{U}_{j+\frac{1}{2}}^-), \lambda_1^c(\mathbf{U}_{j+\frac{1}{2}}^+), 0 \right\} = \min \left\{ V_{max}, \lambda_1^c(\mathbf{U}_{j+\frac{1}{2}}^+), 0 \right\} = \min \left\{ \lambda_1^c(\mathbf{U}_{j+\frac{1}{2}}^+), 0 \right\}. \end{aligned} \quad (3.5) \quad \boxed{3.5a}$$

Notice that in the computation of $a_{j+\frac{1}{2}}^\pm$ in (3.4) and (3.5), we have used the fact that $\lambda_1^c(\mathbf{U}_{j+\frac{1}{2}}^\pm) \leq \lambda_2^c(\mathbf{U}_{j+\frac{1}{2}}^\pm) \leq V_{c+} \leq V_{max}$.

Finally, the term $\mathbf{Q}_{j+\frac{1}{2}}$ in (3.2) represents a “built-in” anti-diffusion and is given by [16]

$$\mathbf{Q}_{j+\frac{1}{2}} = \min \text{mod} \left(\mathbf{U}_{j+\frac{1}{2}}^+ - \mathbf{U}_{j+\frac{1}{2}}^*, \mathbf{U}_{j+\frac{1}{2}}^* - \mathbf{U}_{j+\frac{1}{2}}^- \right),$$

where

$$U_{j+\frac{1}{2}}^* = \frac{a_{j+\frac{1}{2}}^+ U_{j+\frac{1}{2}}^+ - a_{j+\frac{1}{2}}^- U_{j+\frac{1}{2}}^- - \left\{ F(U_{j+\frac{1}{2}}^+) - F(U_{j+\frac{1}{2}}^-) \right\}}{a_{j+\frac{1}{2}}^+ - a_{j+\frac{1}{2}}^-}.$$

The ODE system (3.1)–(3.2) has to be numerically integrated using an appropriate ODE solver. Upon completion of every time step (or every stage of a Runge-Kutta method), we project the obtained set of $(\bar{\rho}_j, \bar{q}_j)$ onto either L_f or Ω_c according to the procedure introduced in §3.1.

3.1 Projection onto L_f or Ω_c

(appc) Assume that we have obtained a set of data (either reconstructed point values or evolved cell averages) for ρ and q . If a certain pair $(\tilde{\rho}, \tilde{q})$ is neither on L_f or in Ω_c , we have to project it onto either L_f or Ω_c according to the following four possible cases:

Case I: If $\tilde{\rho} \leq \rho_{cr}^f$, which means that $\tilde{\rho}$ corresponds to the free flow, we replace \tilde{q} with $q(\tilde{\rho})$ computed using (2.4);

Case II: If $\rho_{cr}^f < \tilde{\rho} < \rho_{cr}^c$ and $\tilde{q} > \frac{\tilde{\rho}\rho_{max}}{\rho_{max} - \tilde{\rho}}V_{c+}$, that is, the point $(\tilde{\rho}, \tilde{q})$ is above the line L_3 (see Figure 2), we shift this point vertically down to L_3 and replace \tilde{q} with $\frac{\tilde{\rho}\rho_{max}}{\rho_{max} - \tilde{\rho}}V_{c+}$;

Case III: If $\rho_{cr}^c < \tilde{\rho}$ and $\tilde{q} > q^* + \frac{q^+ - q^*}{\rho_{max}}\tilde{\rho}$, that is, the point $(\tilde{\rho}, \tilde{q})$ is above the line L_1 (see Figure 2), we shift this point vertically down to L_1 and replace \tilde{q} with $q^* + \frac{q^+ - q^*}{\rho_{max}}\tilde{\rho}$;

Case IV: If $\rho_{cr}^f < \tilde{\rho}$ and $\tilde{q} < q^* + \frac{q^- - q^*}{\rho_{max}}\tilde{\rho}$, that is, the point $(\tilde{\rho}, \tilde{q})$ is below the line L_2 (see Figure 2), we shift this point vertically up to L_2 and replace \tilde{q} with $q^* + \frac{q^- - q^*}{\rho_{max}}\tilde{\rho}$.

Note that in all of these four cases, we modify q only without changing ρ so that vehicles are not getting artificially added or removed from the road.

4 Numerical Examples

(sec4) In this section, we evaluate the performance of the proposed numerical scheme using extensive numerical tests. To this end, we use the three-stage third-order strong stability preserving (SSP) Runge-Kutta method (see, e.g., [10, 11]) in order to numerically solve the ODE system (3.1)–(3.2) using the CFL number 0.4, which is selected based on our initial investigation findings.

For discussion purposes and better organization, we categorize our investigation scenarios into multiple example types according to the similarities between the initial and boundary conditions. In all of our examples, we use the parameters listed in Table 4.1 for the phase-transition model parameters and the physicality constraint parameters for the congested domain. Specifically, q^+ and q^- are selected from a typical range; see, e.g., [20, 27].

Example 1. In the first example, we consider several Riemann initial data of the form

$$U(x, 0) = \begin{cases} U_L & \text{if } x < x_0, \\ U_R & \text{otherwise,} \end{cases} \quad x_0 = 40000,$$

Table 4.1: Parameters of the phase-transition model adopted for numerical tests

Parameter	V_{\max}	V_{c+}	ρ_{\max}	q^*	ρ_{cr}^f	q^+	q^-
Value	30	24	0.16	0.6	0.02	0.93186	0.18856

(tab0)

on the computational domain $[0, 800000]$ subject to free boundary conditions. This setting corresponds to a Riemann problem on a long road with open boundaries.

Test	Left – side				Right – side			
	Phase	ρ_L	V_L	$q_L - q^*$	Phase	ρ_R	V_R	$q_R - q^*$
1	Free	0.011	30	-0.2456	Congested	0.0825	4.5113	0.1684
2	Free	0.011	30	-0.2456	Congested	0.0775	4.5945	0.0906
3	Free	0.0075	30	-0.3639	Congested	0.0675	5.338	2.325e-2
4	Free	0.001	30	-0.5698	Congested	0.0625	4.73	-0.1149
5	Free	0.001	30	-0.5698	Congested	0.0875	2.9945	-2.175e-2
6	Congested	0.128	0.42321	-0.3291	Congested	0.0375	13.838	7.778e-2
7	Congested	0.0375	13.838	7.778e-2	Congested	0.128	0.42321	-0.3291
8	Congested	0.0825	4.5113	0.1684	Free	0.011	30	-0.2456
9	Congested	0.0775	4.5945	0.0906	Free	0.011	30	-0.2456
10	Congested	0.0675	5.338	2.324e-2	Free	0.0075	30	-0.3639
11	Congested	0.0625	4.73	-0.1149	Free	0.001	30	-0.5698
12	Congested	0.0875	2.9945	-2.175e-2	Free	0.001	30	-0.5698

Table 4.2: Initial conditions for Tests 1–12.

(tab1)

Table 4.2 presents the twelve comprehensive test cases defined in our first example, along with the essential information about traffic states on either side of the initial discontinuity. All of these test cases are numerically challenging and can give rise to complex waves, comprising of multiple wave types such as shock waves, contact discontinuities, and rarefaction waves due to involving transitions between the free-flow and congested phases.

In Tests 1–5, free-flow traffic upstream of the initial discontinuity encounters congested traffic downstream. In all of these test cases, vehicles in the upstream will have to decelerate in order to adapt to the traffic condition downstream, and the solution would involve shock waves. While these test cases are quite comparable in terms of traffic speed on either side of the initial discontinuity, there are major differences in terms of drivers' average time gaps (that is, the time taken for a car to travel its available spacing gap to its leading vehicle, which can be calculated as $1/q$). For instance, in Tests 1–2, the quantity $q - q^*$ is negative, suggesting that the drivers' average time gap downstream is less than the equilibrium time gap. Conversely, in Tests 4–5, the positive value of the quantity $q - q^*$ suggests that the drivers' average time gap downstream is smaller than the equilibrium time gap. On the other hand, Test 3 describes a scenario where the average time gap

is very close to the equilibrium one.

Tests 6 and 7 represent scenarios in which there is no phase transition, as the traffic states on both sides of the initial discontinuity are in a congested phase. From a computational and numerical standpoint, these test cases are less challenging. However, they are included for their physical significance, namely, to examine the model's solution structure for Riemann problems where one state's time gap is close to the equilibrium, while the other exhibits a deviation from this equilibrium.

In Tests 8–12, traffic state in the upstream of the initial discontinuity is congested, whereas free-flow traffic exists in the downstream. As a result, vehicles in the upstream will go through acceleration speed adaptation manoeuvres in order to adapt to the traffic condition in the downstream. These cases encompass a variety of transitions between traffic phases, characterized by the fluctuation of the quantity $q - q^*$ across a spectrum of values, from negative to positive. This variation indicates diverse scenarios where drivers' average preferred time gap deviates from the equilibrium time gap, and are considered in the numerical tests for two aspects: (a) to evaluate and demonstrate the performance of the proposed scheme under such complex phase-transitions and (b) to shed light on the phase-transition model's solution structures for such initial discontinuities and provide physical interpretations.

We compute the solutions until the final time $T_{\text{final}} = 900$ by the proposed CU scheme on the computational domain $[0, 40000]$ on the uniform mesh with $\Delta x = 100$ subject to the free boundary conditions. We present the obtained results in Figures 4.1–4.3 together with the reference solution computed on a much finer mesh with $\Delta x = 5$. As one can see, the developed CU scheme can capture the solution structures of these Riemann problems in a non-oscillatory manner and the achieved resolution is high.

Example 2. In the second example, we take computational domain $[0, L]$ with $L = 10000$ and consider the following initial conditions:

$$\rho(x, 0) = \begin{cases} 0.01 & \text{if } x \leq \frac{L}{3}, \\ 0.03 & \text{if } \frac{L}{3} \leq x \leq \frac{2L}{3}, \\ 0.04 & \text{otherwise,} \end{cases} \quad V(x, 0) = \begin{cases} 30 & \text{if } x \leq \frac{L}{3}, \\ 17.729 & \text{if } \frac{L}{3} \leq x \leq \frac{2L}{3}, \\ 11.812 & \text{otherwise,} \end{cases}$$

shown in Figure 4.4 (top row). The corresponding values of the quantity $q - q^*$ are then

$$q(x, 0) - q^* = \begin{cases} -0.2800 & \text{if } x \leq \frac{L}{3}, \\ 0.0546 & \text{if } \frac{L}{3} < x \leq \frac{2L}{3}, \\ 0.0300 & \text{otherwise.} \end{cases}$$

This test case is numerically challenging and physically complex due to the formation and propagation of multiple interacting compound waves traveling in different directions. Specifically, the traffic dynamics vary across the domain: the region $x < \frac{L}{3}$ exhibits free-flowing traffic, which progresses to moderate congestion in the range $\frac{L}{3} < x < \frac{2L}{3}$, and escalates to dense traffic when $x > \frac{2L}{3}$. The initial conditions feature two discontinuities in speed and density profiles. As $q(x, 0) - q^* \neq 0$ for all x , compound waves are anticipated at the interfaces of these discontinuities.

We compute the numerical results using the proposed CU scheme until the final time $T_{\text{final}} = 250$ on a uniform mesh with $\Delta x = 25$ subject to the following Dirichlet boundary conditions

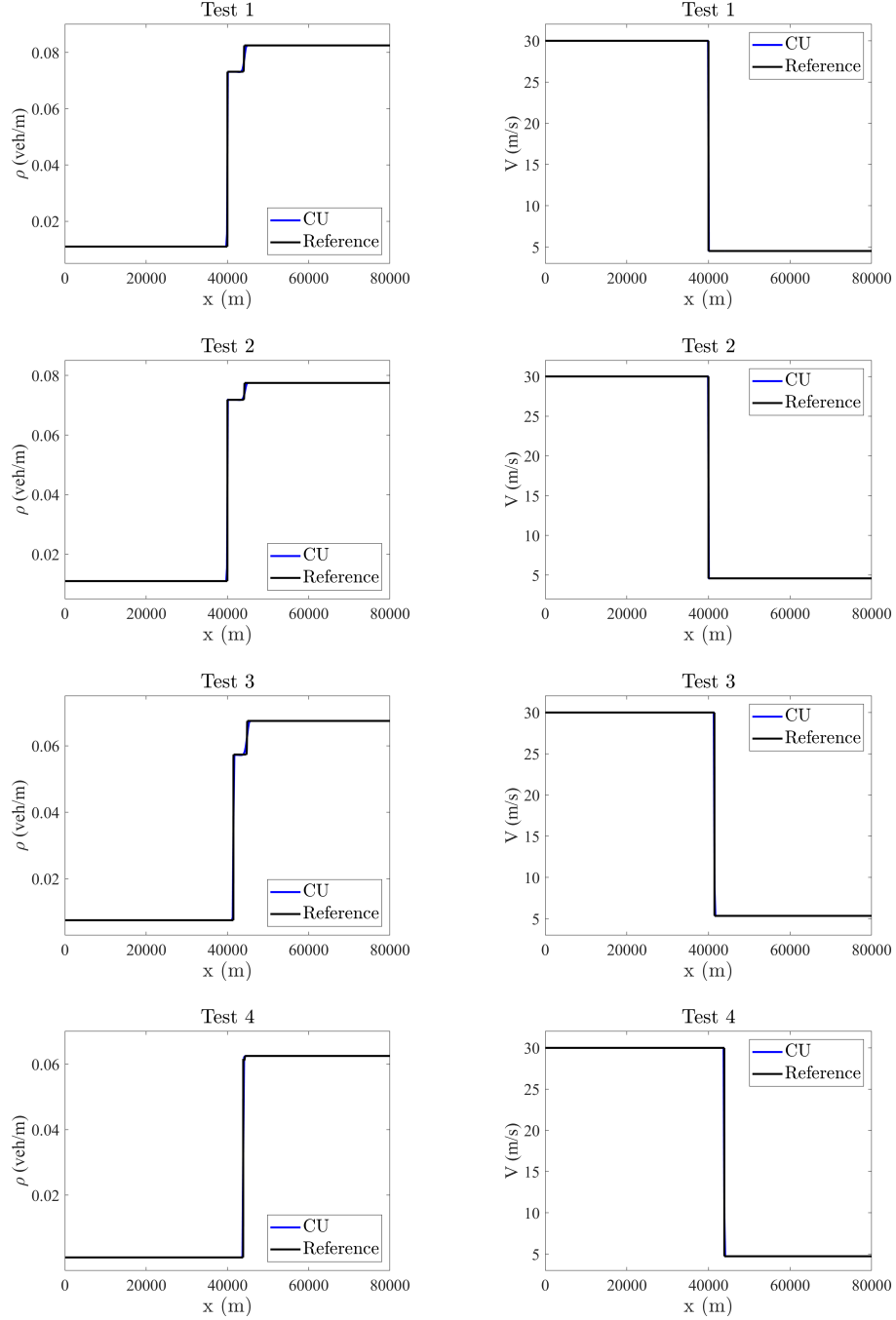


Figure 4.1: Example 1, Tests 1–4: ρ (left column) and V (right column).

(fig41)

imposed at the left end of the computational domain $x = 0$:

$$\rho(0, t) = 0.01, \quad q(0, t) = \frac{\rho(0, t)V_{\max}}{1 - \rho(0, t)/\rho_{\max}},$$

and free boundary conditions at the right end of the computational domain.

The computed ρ and V at times $t = 50, 200$, and 250 are presented in Figure 4.4 together with a reference solution calculated on a finer mesh with $\Delta x = \frac{5}{4}$. The comparison underscores the scheme's robust capability to capture solution structures arising from interacting waves. It

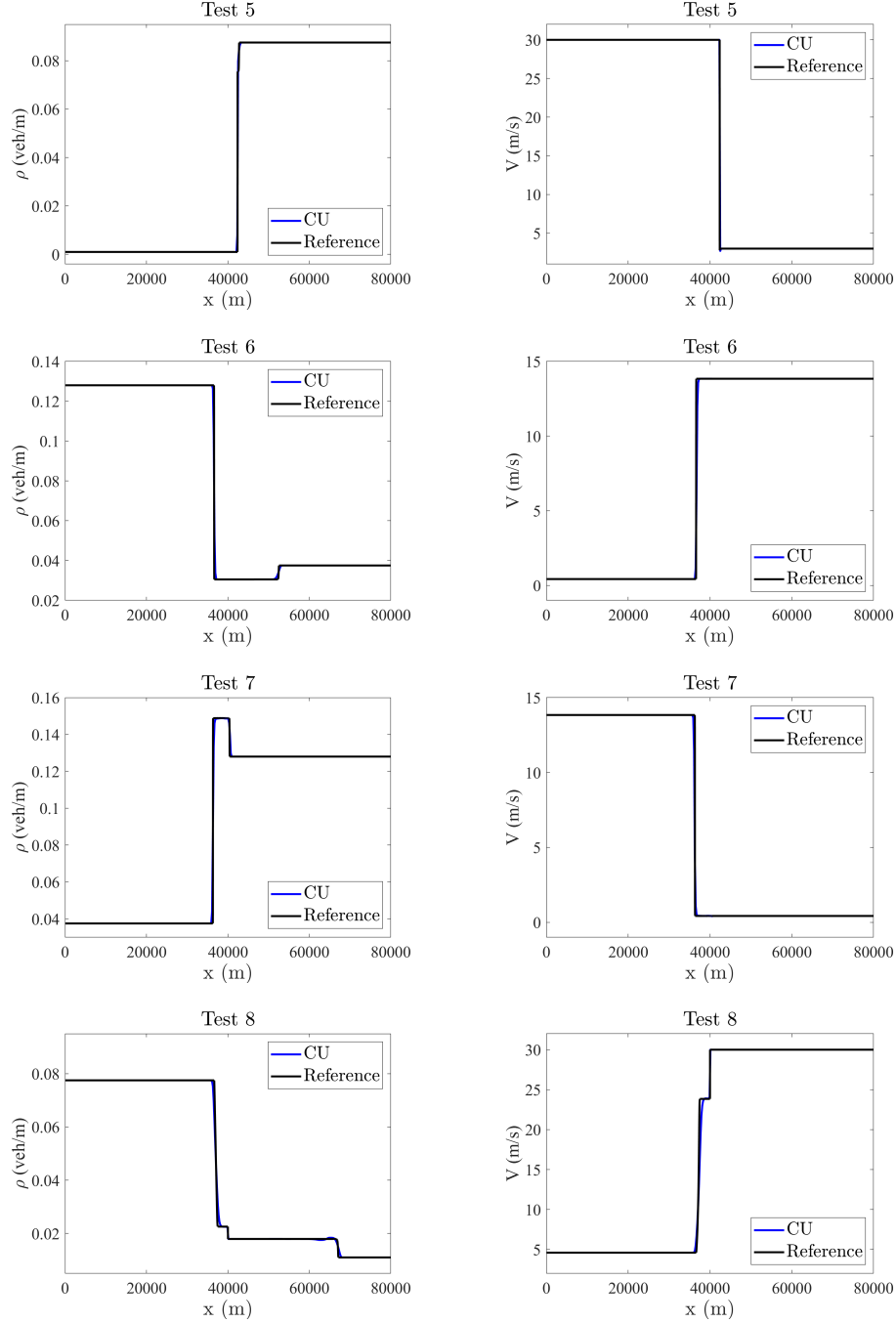


Figure 4.2: Same as in Figure 4.1, but for Tests 5–8.

maintains sharpness near contact discontinuities and shock waves, while ensuring non-oscillatory behavior.

Let us now examine the physical interpretation of the numerical results obtained, as presented in the spatio-temporal evolution of traffic density and speed in Figure 4.5. The spatio-temporal analysis of traffic density indicates that it can be divided into six distinct regions (each characterized by a constant density), which are labeled as A , B , B^* , C , C_1^* , and C_2^* in Figure 4.5 (left). Note that the traffic speed remains invariant across Regions B , B^* , and also across C , C_1^* , and

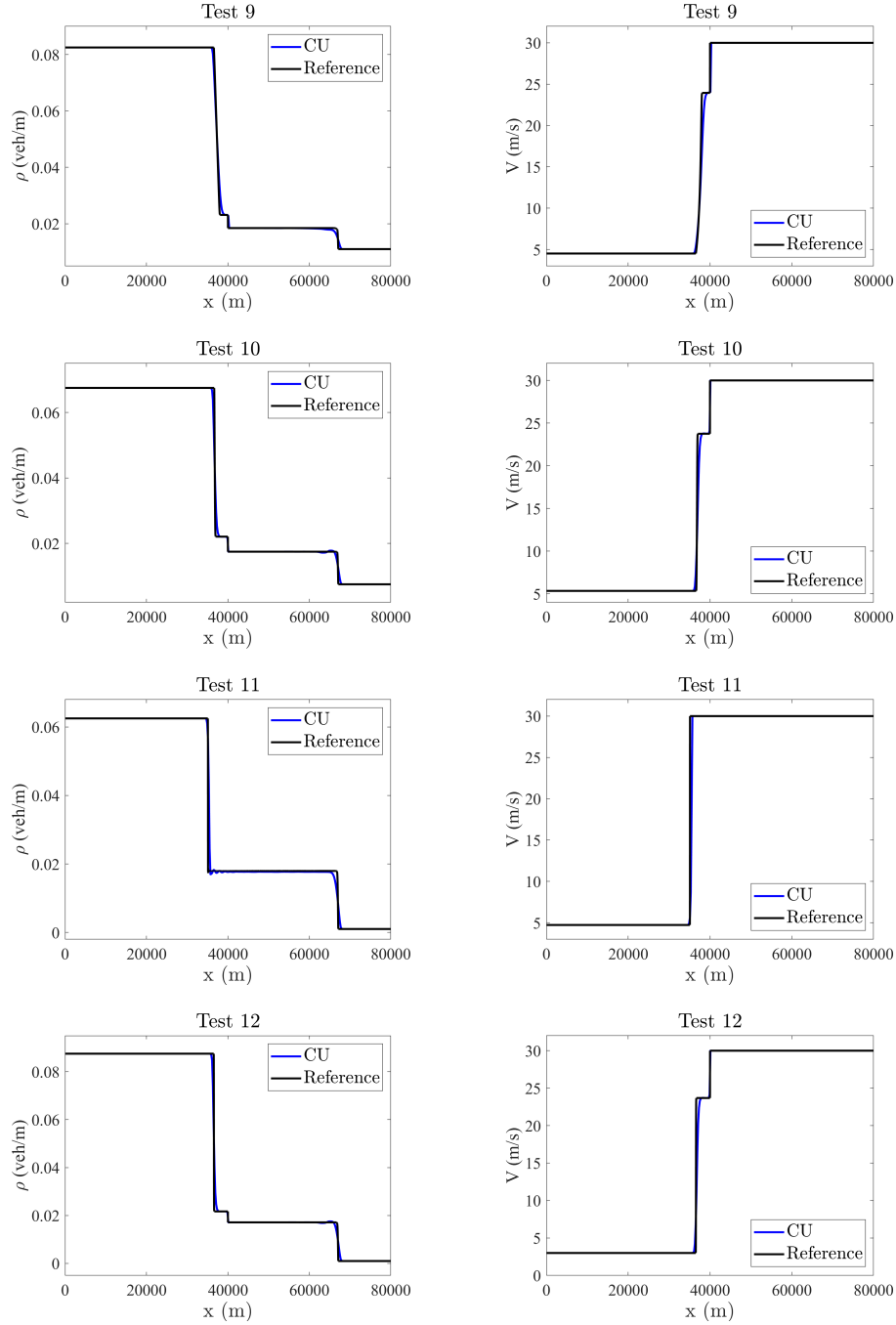
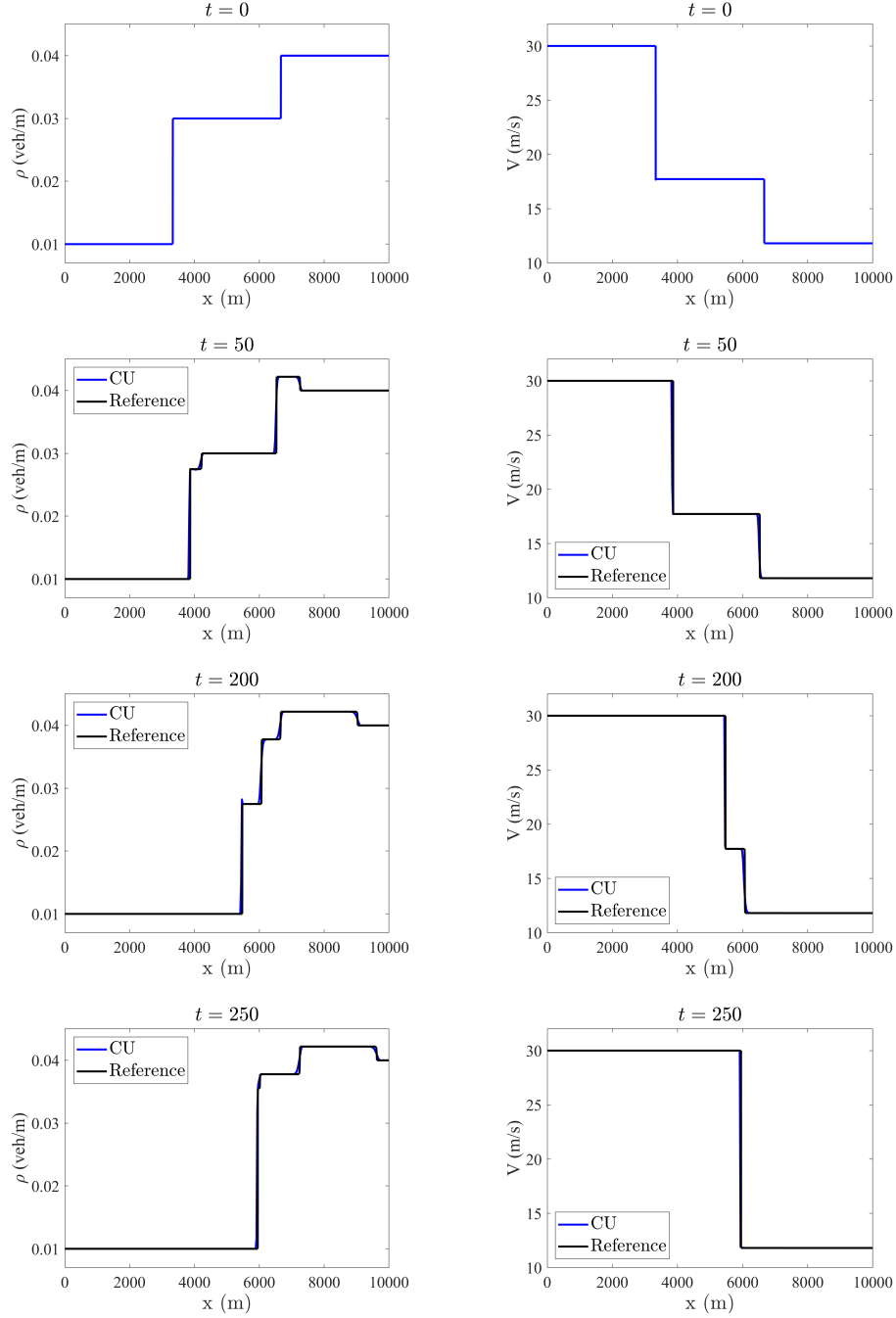


Figure 4.3: Same as in Figure 4.1, but for Tests 9–12.

(fig43)

C_2^* . We shall elaborate on the waves arising at the interface between these regions.

To interpret the results physically, consider the region defined by $\frac{L}{3} < x < \frac{2L}{3}$ in the initial conditions as the reference point, referred to as Region B in Figure 4.5 (left). In Region B, $q(x, 0) - q^* > 0$, suggesting that the inter-vehicular spacing is initially smaller than the equilibrium spacing, and consequently, the traffic density is higher than would be expected with initial $q - q^* = 0$. At time $t = 0$, Region B is flanked upstream by a free-flow region ($x < \frac{L}{3}$, Region A) with very low density, and downstream by a denser traffic condition ($x > \frac{2L}{3}$, Region C). As a result,

Figure 4.4: Example 2: ρ (left column) and V (right column) at different times.

(fig46)

compound waves form at both ends of Region B. To facilitate discussion on these waves, it is important to clarify that henceforth, the endpoints of each region in the spatial domain will be referred to as the right-end (downstream) and left-end (upstream), respectively.

At the left end of Region B, an intermediate state (Region B^*) emerges and separates Regions A and B with a shockwave at the left end of Region B^* (corresponding to λ_1 and traveling forward due to the lower density in Region A) and a contact discontinuity at the right end (corresponding to λ_2). In Region B^* , the traffic speed matches that of Region B, while the density is intermediate between that of Regions A and B. Since the speed of the shockwave is smaller in magnitude

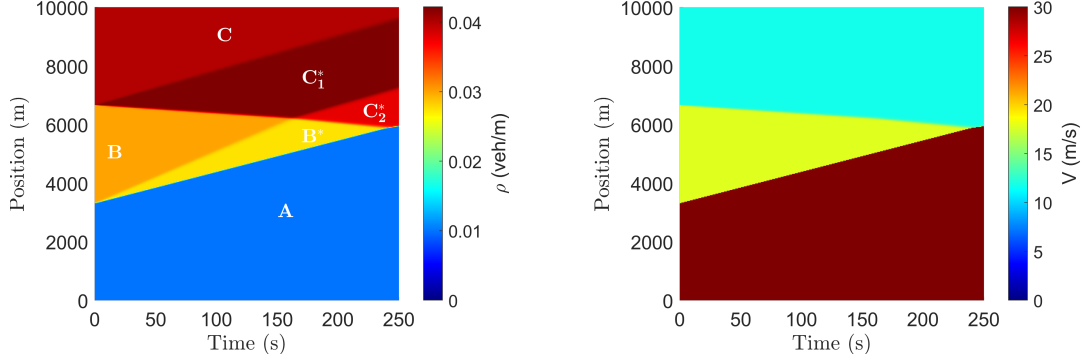


Figure 4.5: Example 2: Spatio-temporal evolution of ρ (left) and V (right).

compared to the speed of the contact discontinuity at the interface between Regions B^* and B , B^* expands spatially over time. This expansion continues until the contact discontinuity ceases to exist around $x = 6200$ m and $t = 160$ s.

At the right end of Region B , another intermediate state, Region C_1^* , emerges, separating Regions B and C . Region C_1^* is characterized by a shockwave at the left end (corresponding to λ_1 and travelling backward due to congestion) and a contact discontinuity at the right end (corresponding to λ_2). Within Region C_1^* , the traffic speed is consistent with that of Region C , while the density is intermediate between those in Regions B and C .

At a specific point in time and space (specifically, around $x = 6200$ m and $t = 160$ s), the shockwave traveling backward at the left end of Region C_1^* meets the contact discontinuity traveling forward at the right end of Region B^* . This interaction leads to the formation of Region C_2^* , which is confined by a shockwave traveling backward and a contact discontinuity traveling forward.

Example 3. In this example, we take the computational domain $[0, L]$ with $L = 10000$ and consider the following initial conditions:

$$\rho(x, 0) = \begin{cases} 0.01 & \text{if } x \leq \frac{L}{3}, \\ 0.03 & \text{if } \frac{L}{3} \leq x \leq \frac{2L}{3}, \\ 0.05 & \text{otherwise,} \end{cases} \quad V(x, 0) = \begin{cases} 30 & \text{if } x \leq \frac{L}{3}, \\ 17.729 & \text{if } \frac{L}{3} \leq x \leq \frac{2L}{3}, \\ 7.941 & \text{otherwise,} \end{cases}$$

presented in Figure 4.6 (top row). The corresponding values of the quantity $q - q^*$ are then

$$q(x, 0) - q^* = \begin{cases} -0.2800 & \text{if } x \leq \frac{L}{3}, \\ 0.0546 & \text{if } \frac{L}{3} < x \leq \frac{2L}{3}, \\ -0.0225 & \text{otherwise.} \end{cases}$$

In this example, free boundary conditions are imposed at the left end of the computational domain, whereas at the right end of the computational domain, we impose the following Dirichlet

boundary conditions:

$$\rho(L, t) = \begin{cases} \rho_0 + \Delta\rho_0 \left(\cosh^{-2} \left(\frac{t - \frac{T_0}{2}}{W^+} \right) - \left(\frac{W^+}{W^-} \right) \cosh^{-2} \left(\frac{t - T_1 - \frac{T_0}{2}}{W^+} \right) \right), & t \leq \frac{2}{3}T_{\text{final}}, \\ \rho_1 + \Delta\rho_1 \left(\cosh^{-2} \left(\frac{t - T_0}{W^+} \right) - \left(\frac{W^+}{W^-} \right) \cosh^{-2} \left(\frac{t - T_1 - T_0}{W^+} \right) \right), & \text{otherwise,} \end{cases}$$

$$q(L, t) = \begin{cases} \frac{3}{4}C_{\text{jam}}\rho_{\text{max}} \left(1 + (a-1) \frac{\rho(L, t)}{\rho_{\text{max}}} - \left[\left(a \frac{\rho(L, t)}{\rho_{\text{max}}} \right)^\theta + \left(1 - \frac{\rho(L, t)}{\rho_{\text{max}}} \right)^\theta \right]^{1/\theta} \right), & \rho(L, t) > \rho_{cr}^f \\ \frac{\rho(L, t)V_{\text{max}}}{1 - \frac{\rho(L, t)}{\rho_{\text{max}}}}, & \text{otherwise.} \end{cases}$$

Here, $\rho_0 = 0.05$, $\Delta\rho_0 = 0.3$, $\rho_1 = 0.03$, $\Delta\rho_1 = 0.2$, $W^+ = 201.25$, $W^- = 805$, $T_0 = 1500$, $T_1 = 3000$, and $T_{\text{final}} = 250$.

While qualitatively similar to previous examples, this case is more complex due to a time-varying downstream boundary condition, leading to the formation of additional wave types and regions. Another key difference is at the interface between the two congestion regions (initially located at $x = \frac{2L}{3}$), where upstream vehicles have smaller inter-vehicular spacing than at equilibrium ($q - q^* > 0$), and downstream vehicles have larger spacing ($q - q^* < 0$). This results in multiple intermediate states and interacting waves, which are challenging to capture, particularly regarding numerical oscillations [4].

We compute the numerical results using the proposed CU scheme until the final time $T_{\text{final}} = 250$ on a uniform mesh with $\Delta x = 25$. The computed values of ρ and V at $t = 50, 200, 350$ and 500 are shown in Figure 4.6 together with a reference solution computed on a finer mesh with $\Delta x = \frac{5}{4}$. As one can see, the scheme accurately captures solution structures from interacting waves while staying sharp near shock waves and contact discontinuities, while remaining non-oscillatory around intermediate states.

To explain the physical interpretation of the numerical results, we consider the spatio-temporal evolution of traffic density and speed, as shown in Figure 4.7. The comparison between speed and density graphs reveals that the solution domain can be divided into four regions where speed is constant; see Figure 4.7 (right). The density in these regions is, however, not constant except for the free-flow Region A. The other regions with constant speed can be further divided into subregions with constant density, labelled as B , B_1^* , C , C_1^* , C_2^* , C_3^* , D , D_1^* , and D_2^* .

To discuss the physical interactions, let us begin with the wave types arising at the initial discontinuities between the three main Regions A, B, and C in the initial condition. The Riemann solution at the left end of Region B involves the formation and expansion of Region B^* between Regions A and B. Region B^* is characterized by a shockwave moving upstream (backward) and a contact discontinuity traveling forward (downstream) at a faster rate than the shockwave. Meanwhile, at $x = 2L/3$ and $t = 0$, one observes the formation of a shockwave traveling backward, causing Region B to shrink, as well as a contact discontinuity traveling forward, which leads to the formation of a high-density intermediate state (Region C_1^*) between Regions B and C.

At approximately $x = 6200$ m and $t = 160$ s, the contact discontinuity at the left end of Region B catches up with the shockwave traveling backward at the right end of Region B, leading to

the formation of Region C_2^* and the clearance of Region B . Region C_2^* spans backward until around $x = 5900$ m and $t = 220$ s, when Region B^* is cleared as the shockwave at the left end of Region B^* meets the contact discontinuity at the right end of Region B^* . This interaction leads to the formation of Region C_3^* , which arises as an intermediate state between another shockwave traveling upstream and a contact discontinuity traveling downstream.

Finally, at $x = L$ and $t = 0$, a shockwave arises travelling backward as the congested state in region C discharges from the downstream, which leads to the formation of another intermediate state between Region C and the downstream boundary (Region D).

At approximately $x = 9000$ m and $t = 280$ s, the shockwave traveling forward at the upper end of region D meets the contact discontinuity traveling forward at the lower end of region C. This interaction forms region D^* , characterized by a compound wave: a contact discontinuity moving forward at the left end of region D_1^* and a shockwave moving upstream at a slightly slower rate at the lower end of region D_1^* .

Region D_1^* persists until approximately $x = 8500$ m and $t = 440$ s, when the shockwave at the lower end of region D_1^* meets the contact discontinuity at the right end of region C_1^* , forming region D_2^* . This leads to another compound wave with a shockwave traveling upstream at the lower end of region D_2^* and a contact discontinuity in region D_2^* .

Example 4. In our final example, we aim to reconstruct a tangible real-world scenario using initial and boundary conditions that are widely observable in real-world traffic. We take the computational domain $[0, L]$ with $L = 10000$ and assume the following initial conditions:

$$\rho(x, 0) = \begin{cases} 0.015 & \text{if } x \leq \frac{L}{2}, \\ 0.08 & \text{if } \frac{L}{2} \leq x \leq \frac{3L}{5}, \\ 0.025 & \text{otherwise,} \end{cases} \quad V(x, 0) = \begin{cases} 30 & \text{if } x \leq \frac{L}{2}, \\ 4.375 & \text{if } \frac{L}{2} \leq x \leq \frac{3L}{5}, \\ 21.94 & \text{otherwise,} \end{cases}$$

presented in Figure 4.8. The corresponding values of the quantity $q - q^*$ are then

$$q(x, 0) - q^* = \begin{cases} -0.1034 & \text{if } x \leq \frac{L}{2}, \\ 0.1 & \text{if } \frac{L}{2} < x \leq \frac{3L}{5}, \\ 0.0501 & \text{otherwise.} \end{cases}$$

The initial conditions in this scenario depict a strong bottleneck with highly congested traffic, represented as an initial queue, in the middle section of a freeway. At the left end of the computational domain, we impose a free upstream boundary condition, while at the right end of the computational domain, we set the following time series of the downstream boundary conditions:

$$\rho(L, t) = \begin{cases} \rho_0 + \Delta\rho_0 \left(\cosh^{-2} \left(\frac{t - T_0}{W^+} \right) - \left(\frac{W^+}{W^-} \right) \cosh^{-2} \left(\frac{t - T_1 - T_0}{W^+} \right) \right), & \text{if } 1000 < t, \\ 0.03, & \text{if } 1000 < t < 1200, \\ 0.01, & \text{otherwise,} \end{cases}$$

$$q(L, t) = \begin{cases} \frac{3}{4} C_{\text{jam}} \rho_{\text{max}} \left(1 + (a - 1) \frac{\rho(L, t)}{\rho_{\text{max}}} - \left[\left(a \frac{\rho(L, t)}{\rho_{\text{max}}} \right)^\theta + \left(1 - \frac{\rho(L, t)}{\rho_{\text{max}}} \right)^\theta \right]^{1/\theta} \right), & \text{if } t < 1200, \\ \frac{\rho(L, t) V_{\text{max}}}{1 - \frac{\rho(L, t)}{\rho_{\text{max}}}}, & \text{otherwise.} \end{cases}$$

which are illustrated in Figure 4.9. Here, $\rho_0 = \Delta\rho_0 = 0.03$, $W^+ = 10.25$, $W^- = 5$, $T_0 = \lfloor \frac{t}{100} \rfloor + 50$, and $T_1 = 3000$.

This scenario is common in real-world traffic. On a homogeneous road without on- or off-ramps, we assume the initial queue in the middle can represent traffic conditions after a crash that occurred at $x = 3L/5$ before the simulation, with the crash scene persisting for a while. This results in very slow queue discharge and light traffic conditions downstream in the area subject to $x > 3L/5$ until the crash scene is cleared at $t = 0$. Additionally, the downstream boundary condition involves stop-and-go traffic up until $t = 1000s$, then transitions to a mildly congested state between $t = 1000s$ and $t = 1200s$, followed by free-flow traffic again for $t > 1200s$. Stop-and-go traffic at the downstream boundary is assumed to result from highly periodic incoming flow through a hypothetical on-ramp further downstream in the computational domain. **Our aim is to investigate the spatiotemporal evolution of traffic flow in a complex scenario involving multiple interacting bottlenecks. This test case provides a good basis for examining these interactions while demonstrating the performance of the proposed scheme and highlighting the physical implications of the results.**

We compute the numerical results using the proposed CU scheme until the final time $t = 2000s$ on a uniform mesh with $\Delta x = 25$. To stay focused, we present only the spatio-temporal evolution of density and speed; see Figure 4.10, which again shows that the proposed scheme can capture the overall structures of the numerical solution in a non-oscillatory manner.

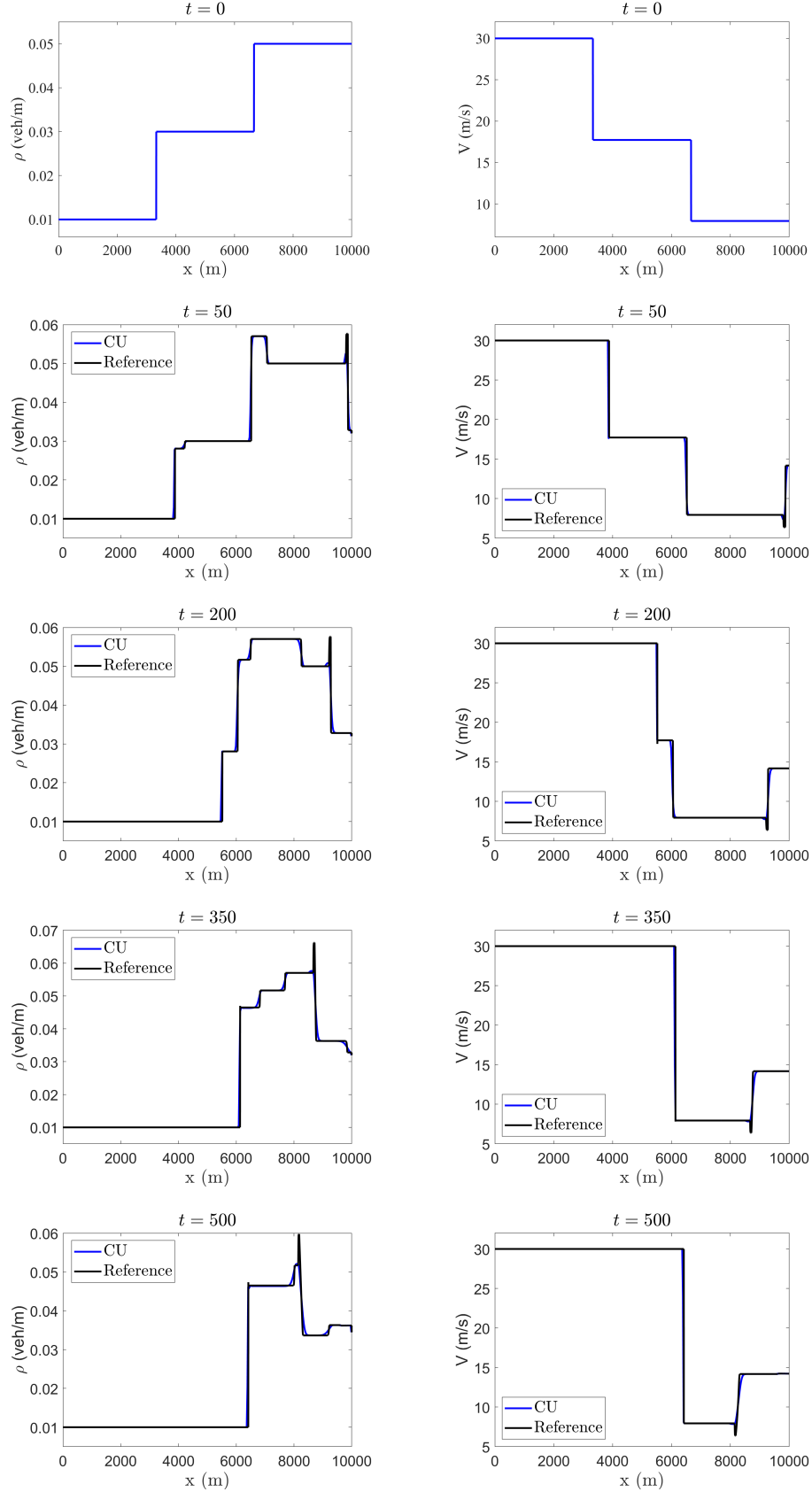
To discuss the results from the physical perspective, we consider the different regions in the density profile as Regions A , B , C_1^* , C_2^* , D , D_1^* , and D_2^* outlined in Figure 4.10 (left). **Region A** pertains to free-flow traffic for all vehicles entering the spatiotemporal domain from the upstream.

First, we focus on the initial queue, highlighted as Region B, which involves a strong bottleneck. Region B is characterized by two backward-traveling shocks at its upper and lower ends. The shockwave at the lower end arises as free-flowing traffic encounters highly congested traffic, whereas the shockwave at the upper end arises as vehicles leave the congestion region. Note that the upper-end shock travels backward faster as vehicles leaving Region B adjust their speed to the maximum in the congested region ($V_{c+} = 24 \text{ m/s}$), and as a result, at around $x = 3800 \text{ m}$ and $t = 600s$, the shockwaves meet, leading to the dissolution of Region B.

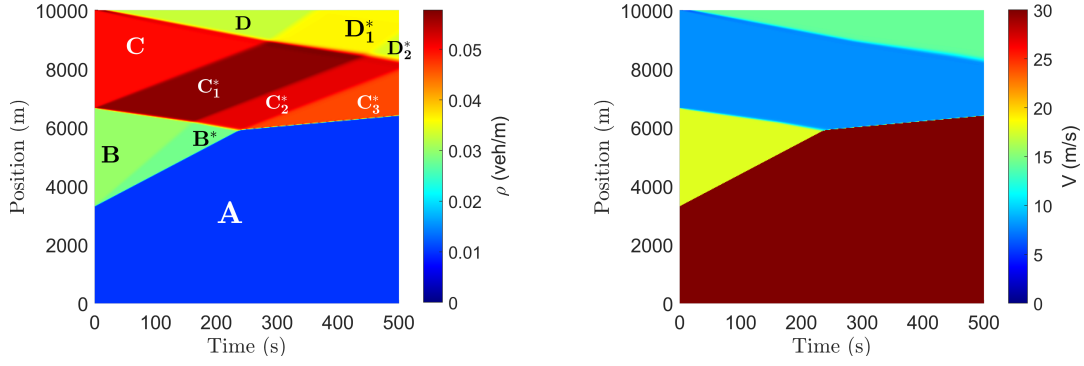
The upper end of Region B neighbors three regions with varying characteristics, as compound waves arise and interact at the interface between the initial queue and free-flow traffic. First, Region C is characterized by a contact discontinuity at its right end. In this region, vehicles maintain their free-flow initial condition. Due to the low traffic density, vehicles in Region C do not create backward-propagating waves when reaching $x = L$, where slow-moving stop-and-go traffic occurs.

Next, Region C_2^* remains congested, with vehicles adapting their speed to the maximum in the congestion domain Ω_c ($V_{c+} = 24 \text{ m/s}$). Region C_2^* is characterized by intermediate congestion, confined by three shocks at its upper, lower, and right ends. The shock at the lower end arises as vehicles leaving the highly congested bottleneck in Region B adjust their speed to the maximum in the congestion domain (i.e., Ω_c). The shock at the right end forms as vehicles from the free-flow Region A enter and pass through C_2^* . The shock at the upper end occurs during the transition from intermediate congestion to the free-flow domain, and as the traffic states neighbouring in the either side of the shock, are in a relatively comparable range. Finally, we have Region C_1^* , where free-flow traffic with a density close to ρ_{cr}^f persists. Region C_1^* is confined by a shock from the lower end, contact discontinuities at the left and right ends, and a backward-traveling shock wave with varying speed at the upper end, which is the interface between Regions C_1^* and D. This shock

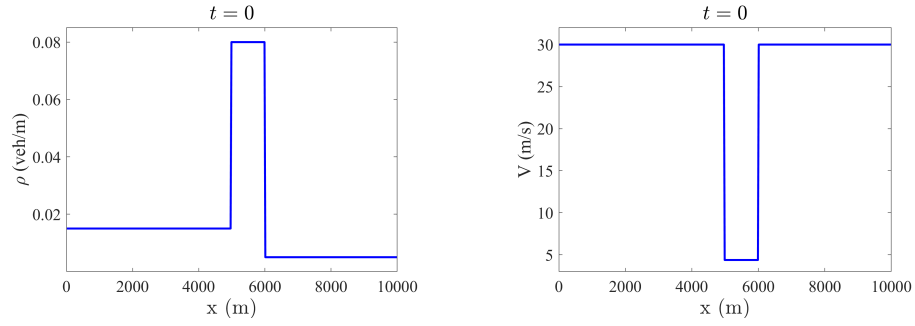
wave arises due to the high traffic flow in Region C_1^* , and upon meeting the congested condition at the downstream boundary (see Figure 4.9), it leads to the formation and backward propagation of the oscillatory Region D. We note that the interface between Regions C_1^* and D has a varying shock speed in the time-space diagram as the tiny cluster-like waves inside Region D also disperse and propagates forward. Region D continues to propagate backward until shortly after Region C_1^* is cleared (roughly at $x = 8300$ m and $t = 1500$ s), at which point the last vehicles leaving Region C_2^* reach Region D. From this point onward, Region A with low density meets Region D from behind, causing the interface between the two regions to become a stationary shock. This stationary shock continue to remain as the downstream boundary condition (at $x = L$) is replaced with a steady congested state during $t \geq 1000$ s and $t \leq 1200$ s. As the downstream boundary condition (at $x = L$) becomes free again for $t > 1200$ s, a new Region D_2^* forms as vehicles in Region D_1^* leave the congested state. A shock wave arises at the interface between Regions D_1^* and D_2^* , traveling backward until it meets the free-flow Region A at approximately $x = 8300$ m and $t = 1650$ s. From this point, a forward-traveling shock wave arises, causing the dissolution of Region D_2^* as vehicles adapt their dynamics to those in Region A.

Figure 4.6: Example 3: ρ (left column) and V (right column) at different times.

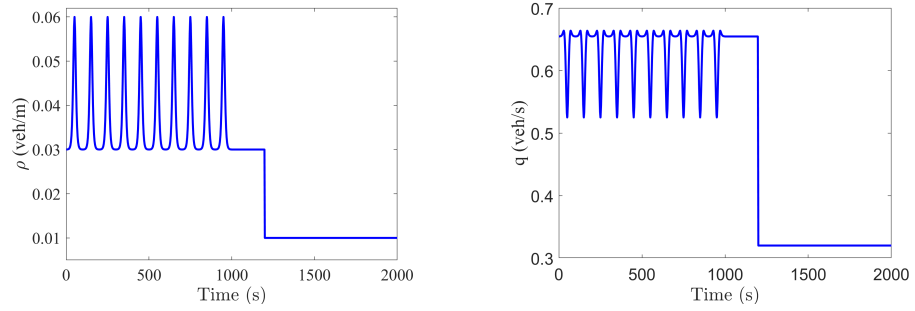
{fig411}

Figure 4.7: Example 3: Spatio-temporal evolution of ρ (left) and V (right).

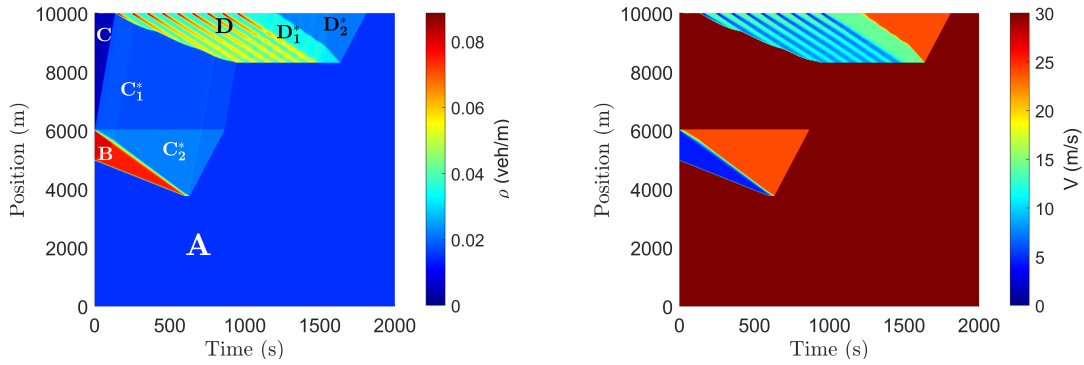
<fig412>

Figure 4.8: Example 4: Initial conditions for ρ (left) and V (right).

<fig413>

Figure 4.9: Example 4: Boundary conditions of ρ at the right end of the computational domain.

<fig413a>

Figure 4.10: Example 4: Spatio-temporal evolution of ρ (left) and V (right).

<fig416>

5 Conclusions

Phase-transition hyperbolic traffic flow models [2,5,7] meet most requirements for non-equilibrium traffic flow models, such as maintaining the anisotropy property, maintaining consistency with the inverse correlation between driver speed and intervehicular spacing, satisfying zero speed at maximum density, and distinctly representing dynamics in free-flow and congested phases. Phase-transition models incorporate “time-gap”, a key element of automated vehicle control logic, as a conserved variable in their equations of state, giving them significant potential for future applications in the era of connected and automated vehicles.

Despite their significant potential, phase-transition models have been largely overlooked in traffic flow theory, particularly in numerical simulations and analysis. This gap is due to the mathematical complexity of these models, such as their discontinuous solution domains and fluxes, which make them challenging to simulate numerically. For instance, previous work on the numerical solution of this model has been very limited, relying on Godunov-type methods that adjust mesh cells and use Glimm-type sampling [3]. However, these methods require solving generalized Riemann problems at each cell interface, significantly increasing computational complexity.

This paper presents the development of a second-order semi-discrete finite-volume central-upwind scheme for the phase-transition traffic flow model. The developed scheme was applied to several challenging numerical examples, demonstrating its ability to capture numerical solution structures sharply and without oscillations. Using this method, the phase-transition model’s performance was studied in various real-world traffic scenarios, where multiple traffic phases interact, leading to interacting bottlenecks and complex solution structures. Such investigations were previously infeasible, but the proposed numerical method now facilitates the implementation of the model in complex real-world traffic scenarios.

There are several future directions for this work. First, future studies can utilize the proposed numerical scheme in conjunction with real-world traffic data to apply optimization-based parameter estimation of the phase-transition model and investigate the performance of the calibrated model against real-world traffic phenomena, as demonstrated in the benchmarking analysis performed by the coauthors of this paper in [20]. Second, the proposed numerical scheme solves traffic flow on homogeneous roads without junctions or interchanges. Future work can extend this freeway-level solver by incorporating boundary coupling conditions at junctions to implement the phase-transition model on complex networks with multiple interacting bottlenecks. Such approaches are crucial for model-predictive optimization of traffic networks. These topics are currently being investigated in ongoing work by the authors.

Acknowledgment

The work of A. Kurganov was supported in part by NSFC grant 12171226 and by the fund of the Guangdong Provincial Key Laboratory of Computational Science and Material Design (No. 2019B030301001).

A Generalized Minmod Reconstruction

⟨appa⟩ In this appendix, we briefly describe a piecewise linear generalized minmod reconstruction [18, 22, 26].

Assume that the cell averages \overline{W}_j of a certain function $W(x)$ are given. We use them to reconstruct a second-order piecewise linear interpolant

$$\widetilde{W}(x) = \overline{W}_j + (W_x)_j(x - x_j), \quad x \in C_j, \quad (\text{A.1}) \quad \boxed{\text{equ3.4}}$$

and then to compute the right- and left-sided point values of W at the cell interfaces $x = x_{j+\frac{1}{2}}$:

$$W_{j+\frac{1}{2}}^- = \overline{W}_j + \frac{\Delta x}{2}(W_x)_j, \quad W_{j+\frac{1}{2}}^+ = \overline{W}_{j+1} - \frac{\Delta x}{2}(W_x)_{j+1}.$$

In order to ensure a non-oscillatory nature of this reconstruction, we compute the slopes $(W_x)_j$ in (A.1) using a generalized minmod limiter:

$$(W_x)_j = \text{minmod} \left(\theta \frac{\overline{W}_j - \overline{W}_{j-1}}{\Delta x}, \frac{\overline{W}_{j+1} - \overline{W}_{j-1}}{2\Delta x}, \theta \frac{\overline{W}_{j+1} - \overline{W}_j}{\Delta x} \right), \quad \theta \in [1, 2], \quad (\text{A.2}) \quad \boxed{\text{equ3.5}}$$

where the minmod function is defined as

$$\text{minmod}(z_1, z_2, \dots) := \begin{cases} \min_j \{z_j\} & \text{if } z_j > 0 \quad \forall j, \\ \max_j \{z_j\} & \text{if } z_j < 0 \quad \forall j, \\ 0 & \text{otherwise.} \end{cases}$$

The parameter θ in (A.2) can be used to control the oscillations: larger θ 's correspond to sharper but, in general, more oscillatory reconstructions.

B Local Characteristic Decomposition

(appb) In order to suppress the oscillations in the piecewise linear reconstruction of ρ and q inside the congested domain, we apply the generalized minmod limiter from Appendix A to the local characteristic variables. To this end, we first introduce the matrix

$$\widehat{A}_{j+\frac{1}{2}} = A(\widehat{\mathbf{U}}_{j+\frac{1}{2}}) = \begin{pmatrix} -\frac{\widehat{q}_{j+\frac{1}{2}}}{\rho_{max}} & \frac{\rho_{max} - \widehat{\rho}_{j+\frac{1}{2}}}{\rho_{max}} \\ \frac{\widehat{q}_{j+\frac{1}{2}}(q^* - \widehat{q}_{j+\frac{1}{2}})}{\widehat{\rho}_{j+\frac{1}{2}}^2} & \frac{(q^* - 2\widehat{q}_{j+\frac{1}{2}})(\widehat{\rho}_{j+\frac{1}{2}} - \rho_{max})}{\widehat{\rho}_{j+\frac{1}{2}}\rho_{max}} \end{pmatrix},$$

where $A = \frac{\partial \mathbf{F}}{\partial \mathbf{U}}$, $\widehat{\rho}_{j+\frac{1}{2}} = \frac{\bar{\rho}_j + \bar{\rho}_{j+1}}{2}$ and $\widehat{q}_{j+\frac{1}{2}} = \frac{\bar{q}_j + \bar{q}_{j+1}}{2}$, and construct the matrix, which consists of the two eigenvectors of $\widehat{A}_{j+\frac{1}{2}}$:

$$R_{j+\frac{1}{2}} = \begin{pmatrix} \frac{\widehat{\rho}_{j+\frac{1}{2}}}{\widehat{q}_{j+\frac{1}{2}} - q^*} & \frac{\widehat{\rho}_{j+\frac{1}{2}}(\rho_{max} - \widehat{\rho}_{j+\frac{1}{2}})}{\widehat{C}_{j+\frac{1}{2}}} \\ 1 & 1 \end{pmatrix}.$$

We then compute its inverse

$$R_{j+\frac{1}{2}}^{-1} = \begin{pmatrix} \frac{\widehat{q}_{j+\frac{1}{2}}(\widehat{q}_{j+\frac{1}{2}} - q^*)\rho_{max}}{\widehat{\rho}_{j+\frac{1}{2}}(\widehat{q}_{j+\frac{1}{2}}\widehat{\rho}_{j+\frac{1}{2}} + q^*(\rho_{max} - \widehat{\rho}_{j+\frac{1}{2}}))} & \frac{(\widehat{q}_{j+\frac{1}{2}} - q^*)(\widehat{\rho}_{j+\frac{1}{2}} - \rho_{max})}{\widehat{q}_{j+\frac{1}{2}}\widehat{\rho}_{j+\frac{1}{2}} + q^*(\rho_{max} - \widehat{\rho}_{j+\frac{1}{2}})} \\ \frac{\widehat{q}_{j+\frac{1}{2}}(q^* - \widehat{q}_{j+\frac{1}{2}})\rho_{max}}{\widehat{\rho}_{j+\frac{1}{2}}(\widehat{q}_{j+\frac{1}{2}}\widehat{\rho}_{j+\frac{1}{2}} + q^*(\rho_{max} - \widehat{\rho}_{j+\frac{1}{2}}))} & \frac{\widehat{q}_{j+\frac{1}{2}}\rho_{max}}{\widehat{q}_{j+\frac{1}{2}}\widehat{\rho}_{j+\frac{1}{2}} + q^*(\rho_{max} - \widehat{\rho}_{j+\frac{1}{2}})} \end{pmatrix}$$

and introduce the local characteristic variables $\mathbf{\Gamma}$ in the neighborhood of $x = x_{j+\frac{1}{2}}$:

$$\mathbf{\Gamma}_k = R_{j+\frac{1}{2}}^{-1} \bar{\mathbf{U}}_k, \quad k = j-1, j, j+1, j+2.$$

Finally, we compute the slopes $(\mathbf{\Gamma}_x)_j$ using the generalized minmod limiter (A.2) applied to $\mathbf{\Gamma}$ in a componentwise manner, evaluate the point values of $\mathbf{\Gamma}$:

$$\mathbf{\Gamma}_{j+\frac{1}{2}}^- = \mathbf{\Gamma}_j + \frac{\Delta x}{2} (\mathbf{\Gamma}_x)_j \quad \text{and} \quad \mathbf{\Gamma}_{j+\frac{1}{2}}^+ = \mathbf{\Gamma}_{j+1} - \frac{\Delta x}{2} (\mathbf{\Gamma}_x)_{j+1},$$

and end up with obtaining the corresponding point values of \mathbf{U} :

$$\mathbf{U}_{j+\frac{1}{2}}^\pm = R_{j+\frac{1}{2}} \mathbf{\Gamma}_{j+\frac{1}{2}}^\pm.$$

References

- [in2013phase](#) [1] S. BLANDIN, J. ARGOTE, A. M. BAYEN, AND D. B. WORK, *Phase transition model of non-stationary traffic flow: Definition, properties and solution method*, Transport. Res. Part B-Meth, 52 (2013), pp. 31–55.
- [2011general](#) [2] S. BLANDIN, D. B. WORK, P. GOATIN, B. PICCOLI, AND A. M. BAYEN, *A general phase transition model for vehicular traffic*, SIAM J. Appl. Math., 71 (2011), pp. 107–127.
- [2008godunov](#) [3] C. CHALONS AND P. GOATIN, *Godunov scheme and sampling technique for computing phase transitions in traffic flow modeling*, Interface. Free. Bound., 10 (2008), pp. 197–221.
- [CKMZ23](#) [4] S. CHU, A. KURGANOV, S. MOHAMMADIAN, AND Z. ZHENG, *Fifth-order A-WENO path-conservative central-upwind scheme for behavioral non-equilibrium traffic models*, Commun. Comput. Phys., 33 (2023), pp. 692–732.
- [Colombo02](#) [5] R. M. COLOMBO, *A 2×2 hyperbolic traffic flow model*, Math. Comput. Modelling, 35 (2002), pp. 141–163.
- [Colombo02a](#) [6] R. M. COLOMBO, *Hyperbolic phase transitions in traffic flow*, SIAM J. Appl. Math., 63 (2002), pp. 708–721.
- [CG14](#) [7] R. M. COLOMBO AND M. GARAVELLO, *Phase transition model for traffic at a junction*, J. Math. Sci. (N.Y.), 196 (2014), pp. 30–36.
- [1995requiem](#) [8] C. DAGANZO, *Requiem for second-order fluid approximations of traffic flow*, Transport. Res. B-Meth., 29 (1995), pp. 277–286.
- [don9](#) [9] W. S. DON, D.-M. LI, Z. GAO, AND B.-S. WANG, *A characteristic-wise alternative WENO-Z finite difference scheme for solving the compressible multicomponent non-reactive flows in the overestimated quasi-conservative form*, J. Sci. Comput., 82 (2020). Paper No. 27, 24 pp.
- [Gottlieb11](#) [10] S. GOTTLIEB, D. KETCHESON, AND C.-W. SHU, *Strong stability preserving Runge-Kutta and multistep time discretizations*, World Scientific Publishing Co. Pte. Ltd., Hackensack, NJ, 2011.

- Gottlieb12 [11] S. GOTTLIEB, C.-W. SHU, AND E. TADMOR, *Strong stability-preserving high-order time discretization methods*, SIAM Rev., 43 (2001), pp. 89–112.
- JSZ [12] Y. JIANG, C.-W. SHU, AND M. ZHANG, *An alternative formulation of finite difference weighted ENO schemes with Lax-Wendroff time discretization for conservation laws*, SIAM J. Sci. Comput., 35 (2013), pp. A1137–A1160.
- Joh [13] E. JOHNSEN, *On the treatment of contact discontinuities using WENO schemes*, J. Comput. Phys., 230 (2011), pp. 8665–8668.
- 016failure [14] B. S. KERNER, *Failure of classical traffic flow theories: Stochastic highway capacity and automatic driving*, Physica. A., 450 (2016), pp. 700–747.
- Kurganov01 [15] A. KURGANOV, S. NOELLE, AND G. PETROVA, *Semidiscrete central-upwind schemes for hyperbolic conservation laws and Hamilton-Jacobi equations*, SIAM J. Sci. Comput., 23 (2001), pp. 707–740.
- Kurganov07 [16] A. KURGANOV AND C.-T. LIN, *On the reduction of numerical dissipation in central-upwind schemes*, Commun. Comput. Phys., 2 (2007), pp. 141–163.
- Kurganov00 [17] A. KURGANOV AND E. TADMOR, *New high-resolution semi-discrete central schemes for Hamilton-Jacobi equations*, J. Comput. Phys., 160 (2000), pp. 720–742.
- lie03 [18] K.-A. LIE AND S. NOELLE, *On the artificial compression method for second-order nonoscillatory central difference schemes for systems of conservation laws*, SIAM J. Sci. Comput., 24 (2003), pp. 1157–1174.
- Liu17 [19] H. LIU, *A numerical study of the performance of alternative weighted ENO methods based on various numerical fluxes for conservation law*, Appl. Math. Comput., 296 (2017), pp. 182–197.
- enchmarking [20] S. MOHAMMADIAN, Z. ZHENG, MD. M. HAQUE, AND A. BHASKAR, *Performance of continuum models for realworld traffic flows: Comprehensive benchmarking*, Transport. Res. B-Meth., 147 (2021), pp. 132–167.
- 3continuum [21] S. MOHAMMADIAN, Z. ZHENG, MD. M. HAQUE, AND A. BHASKAR, *Continuum modeling of freeway traffic flows: State-of-the-art, challenges and future directions in the era of connected and automated vehicles*, Commun. Transp. Res., 3 (2023). Paper No. 100107, 25 pp.
- Nessyahu90 [22] H. NESSYAHU AND E. TADMOR, *Nonoscillatory central differencing for hyperbolic conservation laws*, J. Comput. Phys., 87 (1990), pp. 408–463.
- Nonomura20 [23] T. NONOMURA AND K. FUJII, *Characteristic finite-difference WENO scheme for multicomponent compressible fluid analysis: overestimated quasi-conservative formulation maintaining equilibriums of velocity, pressure, and temperature*, J. Comput. Phys., 340 (2017), pp. 358–388.
- Qiu02 [24] J. QIU AND C.-W. SHU, *On the construction, comparison, and local characteristic decomposition for high-order central WENO schemes*, J. Comput. Phys., 183 (2002), pp. 187–209.

- [Shu20] [25] C.-W. SHU, *Essentially non-oscillatory and weighted essentially non-oscillatory schemes*, Acta Numer., 5 (2020), pp. 701–762.
- [Sweby84] [26] P. K. SWEBY, *High resolution schemes using flux limiters for hyperbolic conservation laws*, SIAM J. Numer. Anal., 21 (1984), pp. 995–1011.
- [r2010three] [27] M. TREIBER, A. KESTING, AND D. HELBING, *Three-phase traffic theory and two-phase models with a fundamental diagram in the light of empirical stylized facts*, Transport. Res. B-Meth., 44 (2010), pp. 983–1000.
- [wang18] [28] B.-S. WANG, P. LI, Z. GAO, AND W. S. DON, *An improved fifth order alternative WENO-Z finite difference scheme for hyperbolic conservation laws*, J. Comput. Phys., 374 (2018), pp. 469–477.